

Turbulent flow over water waves in the presence of stratification

Peter P. Sullivan

National Center for Atmospheric Research, P.O. Box 3000, Boulder, Colorado 80307-3000

James C. McWilliams

Department of Atmospheric Sciences and Institute of Geophysics and Planetary Physics, University of California–Los Angeles, Los Angeles, California 90095-1565
and National Center for Atmospheric Research, P.O. Box 3000, Boulder, Colorado 80307-3000

(Received 7 August 2001; accepted 11 December 2001)

Direct numerical simulation is used to investigate stratified turbulent flow over a series of prescribed moving water waves at a bulk Reynolds number $Re=8000$ and waveslope $ak=0.1$. Unstable, neutral, and stable stratifications are considered for a range of wave phase speeds c . Stratification is shown to significantly alter the mean vertical profiles of velocity and temperature, turbulence variances, wave-induced flow fields, and surface form stress. For the range of conditions considered, the surface form stress (drag) and flow patterns (critical-layer height and streamlines) are well correlated with the friction velocity u_* , which therefore contains the essential information about stratification influences. Nonseparated sheltering [Belcher and Hunt, *Annu. Rev. Fluid. Mech.* **30**, 507 (1998)], which determines the drag in neutral flow over stationary topography, is modified by stratification and the movement of the underlying waves. The variation of the form stress with phase speed is correlated with the movement of the critical layer above the surface. Compared to neutral flow at a given phase speed, the flow patterns with unstable stratification are similar to the flow patterns over slower moving waves while stable stratification results in flow patterns typical of faster moving waves. This behavior is qualitatively captured by the wave age parameter c/u_* . The wave-induced temperature field responds to the wave-induced velocity fields by forming positive and negative patches over the wave crests and troughs, respectively, with the resulting wave-induced heat flux as much as 15% of the total surface heat flux. Estimates of wave growth from the DNS are in reasonable agreement with field observations and laboratory experiments, and they are larger than predictions from high Reynolds-number, second-order closure models for $c/u_* < 10$. For $c/u_* > 10$, the present calculations predict less negative form stress (or less damping) of the waves compared to second-order closure models. © 2002 American Institute of Physics.
[DOI: 10.1063/1.1447915]

I. INTRODUCTION

Coupling between the atmosphere and ocean occurs at the air–sea interface where numerous mechanic (momentum transfer) and thermodynamic (sensible and latent heat transfer) interactions take place. One of the most important and visible components of air–sea interaction is the coupling of water waves and atmospheric turbulence. Since turbulence in the surface layer of the planetary boundary layer is affected by buoyancy forces we expect density stratification to play a role in air-wave coupling dynamics.

There is extensive literature on neutrally stratified air flow over waves and stationary hills, both experimental and computational. Belcher and Hunt¹ provide a review of the current state of second-order closure modeling, while Belcher *et al.*² and Belcher and Hunt,³ emphasizing a triple deck analysis of the turbulent flow, discuss the physical mechanisms that contribute to the flow patterns and form (pressure) drag. In the case of low amplitude hills (no flow separation), they find that the action of turbulent stresses on the mean flow close to the surface thickens the boundary layer on the leeside of a hill leading to an asymmetrical flow pattern and hence drag (referred to as non-separated shelter-

ing). In flow over water waves sheltering continues to dominate, but the physical picture is further complicated by the movement of the underlying surface and the presence of a critical layer.^{1,4,5}

In flow over hills, Hunt *et al.*⁶ find that the flow patterns away from the surface are considerably altered by stable stratification while Belcher and Wood⁷ discuss the impact of stratification on form drag. The few theoretical studies that examine the effect of stratification on wave growth use analytic models based on the Taylor–Goldstein equation⁸ or second-order closure models.⁹ Accounting for the density stratification of the atmosphere is important and has been shown to help explain scatter in observed wave growth in field observations.¹⁰ There are also a few experimental studies in wind-wave tank facilities that specifically focused on the impact of stratification and flow over water waves. Papadimitrakis *et al.*^{11,12} found that the effects of stratification in the mean velocity and temperature profiles over water waves can be accounted for by comparing profiles at the same nondimensional height, z^+ ,¹³ above the waves and that the bulk aerodynamic coefficients for heat and mass transfer are best correlated with the friction velocity. Their proposal

to use friction velocity scaling is consistent with the physical interpretation of Voorrips *et al.*⁹ that the main influence of stratification in flow over water waves is to change the turbulence intensity.

Previously, we used three-dimensional, time-dependent, direct numerical simulation (DNS) to study the interaction between neutrally stratified turbulence and an idealized surface gravity wave field under Couette flow.⁴ Our simulations show that the turbulent flow above moving waves generates an asymmetrical flow about the wave crest, similar to flow over hills, but the mean streamline patterns further depend on the phase speed of the wave and the presence of a critical layer. In the DNS, the surface pressure field and form stress (drag) variations with wave age are similar to predictions from rough-wall second-order closure models despite the huge difference in Reynolds number. The present paper builds on our previous DNS investigation and examines the interaction between an imposed surface gravity wave field and stratified turbulence for varying wave age. We are particularly interested in the surface pressure and the behavior of the flow in the vicinity of the moving wavy surface.

In related work, there are a few turbulence-resolving simulations of neutrally stratified flow above stationary topography, e.g., Cherukat *et al.*¹⁴ and Calhoun and Street.¹⁵ These studies focus on steep topography and the turbulence mechanisms present in separated flows. Separation occurs for a waveslope greater than about 0.3 depending on the surface roughness.¹⁶ We consider smooth surfaces with small waveslopes of 0.1 (see Sec. IV) and hence separation is not an important influence. Heated Couette flow, which we describe below, has frequently served as an idealized flow model for studying turbulence under the driving influences of both shear and buoyancy (but without surface waves), with particular attention to the criteria for the formation of longitudinal convective rolls. Domaradzki and Metcalfe¹⁷ used DNS (smooth boundaries) to examine sheared convection at Rayleigh numbers of order 1.5×10^5 , while Sykes and Henn¹⁸ considered a similar flow using large-eddy simulation (LES) with parameterized surface roughness. Both sets of investigators found that shear tends to organize the convective flow into near two-dimensional rolls with axis parallel to the mean flow direction. In the LES, the strength and pattern of the organized streamwise rolls is well correlated with the ratio of the friction velocity to the convective velocity scale u_* / w_* ; roll formation occurs for $u_* / w_* > 0.35$. These numerical studies all consider flat upper and lower boundaries. Krettenauer and Schumann,^{19,20} using both DNS and LES, include a stationary wavy lower boundary in their simulations but only consider Rayleigh–Bénard convection (i.e., with no mean wind). They identify a critical wavelength of the surface undulation that produces rolls with axes in directions both parallel and perpendicular to the wave crests.

II. PROBLEM FORMULATION

The geophysical flow of interest is modeled as a three-dimensional, stratified, turbulent, viscous, Couette flow over a series of heated (or cooled) two-dimensional water waves (Fig. 1). The coordinate system is such that x is aligned with

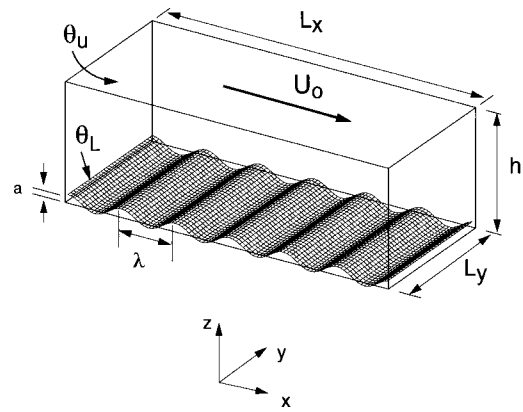


FIG. 1. Sketch of 3D stratified Couette flow driven by velocity U_0 over a moving wavy boundary of wavelength λ (wave number $k=2\pi/\lambda$), phase speed c , and amplitude a in a domain of size $(L_x, L_y, h)=(6, 4, 1)\lambda$. The surface temperature of the wave and upper boundary are θ_L and θ_U , respectively.

the primary flow direction, y is parallel to the wave crests, and z is measured vertically from the mean water surface. The corresponding velocity components are (u, v, w) , pressure is p , and the fluid temperature, viscosity, density, and thermal conductivity are $(\theta, \nu, \rho, \alpha)$, respectively. In the present problem the water wave is assumed to be a two-dimensional, monochromatic, deep-water gravity wave with: wavelength λ , phase speed c , amplitude a , waveslope $ak = a2\pi/\lambda$, where the wave number $k=2\pi/\lambda$, and orbital velocities given by first-order wave theory. The external forcing of the flow occurs through a constant velocity U_0 imposed at $z=h$ and a thermal gradient $\Delta\theta = \theta_L - \theta_U$ where the constant temperatures of the water surface and upper boundary are θ_L and θ_U .

The governing equations for this flow are the Navier–Stokes equations for a Boussinesq fluid written in nondimensional form:

$$\begin{aligned} \frac{\partial u_i}{\partial t} + \frac{\partial u_i u_j}{\partial x_j} &= -\frac{\partial p}{\partial x_i} - Ri(\theta - \theta_o)\delta_{3i} + \frac{1}{Re} \frac{\partial^2 u_i}{\partial x_j^2}, \\ \frac{\partial \theta}{\partial t} + \frac{\partial \theta u_j}{\partial x_j} &= \frac{1}{Pr Re} \frac{\partial^2 \theta}{\partial x_j^2}, \\ \frac{\partial u_i}{\partial x_i} &= 0, \end{aligned} \quad (1)$$

where length, time, velocity, and temperature are appropriately made dimensionless by $(h, h/U_0, U_0, \Delta\theta)$. Then the dimensionless parameters are the Reynolds number $Re = U_0 h / \nu$, Prandtl number $Pr = \nu / \alpha$, and Richardson number

$$Ri = -\frac{gh}{\theta_o} \frac{\Delta\theta}{(\Delta U)^2}, \quad (2)$$

where θ_o is a reference temperature and $\Delta(\theta, U)$ denote jumps in temperature and velocity between the upper and lower walls (Fig. 1). Our normalization and sign convention in Eq. (2) are chosen so that the regimes of unstable, neutral, and stable stratification correspond to $Ri < 0, = 0, > 0$, respectively. To simulate neutrally stratified flow, a finite $\Delta\theta$ is

imposed, but the buoyancy term in the vertical momentum equation is omitted so that θ is then simply a passive scalar. ($h, U_o, \Delta\theta$) are also used to nondimensionalize the properties of the imposed wave. Thus, when we refer to the phase speed of the wave c it is understood that it is nondimensionalized by U_o .

Boundary conditions are imposed consistent with a typical DNS, i.e., periodic (in x and y) sidewalls and no slip conditions in the vertical direction. At the surface the air velocities and fluid temperature are matched to the orbital velocities of the wave and the surface temperature, while at the upper boundary $(u, v, w) \rightarrow (U_o, 0, 0)$ and $\theta \rightarrow \theta_U$.

III. NUMERICAL METHOD

The numerical method used to solve the continuity, momentum, and temperature transport equations is fully described by Sullivan *et al.*⁴ and thus is only briefly outlined here. Our method uses a conformal (hence orthogonal) mapping to transform the Cartesian coordinates (x, y, z) into a flat computational space (ξ, η, ζ) . A co-located grid architecture is used for all variables instead of a staggered layout typical of most numerical schemes. We use contravariant “flux” velocities²¹ at the cell faces and adopt the momentum-interpolation method of Rhie and Chow²² to maintain close velocity-pressure coupling. This procedure has the additional advantage that large bends in the physical coordinate lines can be accommodated.

In our co-located DNS, the spatial differencing and time advancement are similar to our large-eddy simulation code;²³ pseudo-spectral differencing in (ξ, η) planes and second-order finite differences in the transformed ζ direction are used and the time stepping is accomplished with a third-order explicit Runge–Kutta method using a fixed CFL criterion. A nonuniform vertical (ζ) mesh is used to resolve the top and bottom boundary layers in our viscous Couette flow; constant spacing is used in (ξ, η) directions. Because of the coordinate transformation, the Poisson equation for the pressure contains variable coefficients and is solved using an iterative method, approximately 10 iterations are required to converge the pressure solution. At each time step mass divergence is satisfied to machine zero. Finally, to take out the temporal variation of the lower boundary, $z_{bdy} = a \cos[k(x - ct)]$, solutions are obtained in a frame of reference moving at the wave phase speed c .

IV. DNS EXPERIMENTS

The posed problem has a large parameter space to explore: variations in phase speed c , waveslope ak , Reynolds, and Richardson numbers are all of interest. To conserve computational resources, we concentrate on fixed values of waveslope $ak=0.1$ and $Re=8000$ (whose sensitivities are examined in Sullivan *et al.*,⁴ for neutral stratification), and we vary the phase speed c and Richardson number. Simulations with a flat stationary lower boundary ($ak=0, c=0$) are also performed to establish a baseline for the effects of stratification. The results presented here are drawn from a database of more than 20 simulations (Table I).

TABLE I. Simulation properties.

c/U_o	Ri	D_p/u_*^2	$u_* \times 10^2$	$q_* \times 10^3$
0.	-0.031	0.138	3.58	1.25
0.	0	0.129	3.21	1.03
0.	0.031	0.112	2.66	0.698
0.062	-0.031	0.156	3.410	1.148
0.062	0	0.139	3.280	1.076
0.062	0.031	0.117	2.561	0.647
0.125	-0.031	0.190	3.619	1.282
0.125	0	0.181	3.200	1.024
0.125	0.031	0.164	2.789	0.774
0.25	-0.094	0.191	4.102	1.621
0.25	-0.031	0.174	3.647	1.304
0.25	0	0.123	3.179	1.01
0.25	0.031	0.104	2.758	0.750
0.365	-0.031	0.049	3.547	1.234
0.365	0	0.022	3.170	1.005
0.365	0.031	0.00237	2.635	0.687
0.50	-0.031	-0.0072	3.444	1.179
0.50	0	-0.016	3.081	0.949
0.50	0.031	-0.0312	2.538	0.643
0.70	-0.031	-0.0250	3.400	1.154
0.70	0	-0.0350	3.080	0.948

At $Re=8000$, turbulence is well developed in neutral Couette flow since this value is well beyond the transitional value ($Re=2000$) reported by Bech *et al.*²⁴ The corresponding wall Reynolds number, $Re_* = u_* h / 2\nu$, varies from about 100 to 164 over the range of stratification and phase speed considered. These values are 2 to 3 times greater than the values used by Komminaho *et al.*²⁵ and Bech *et al.*²⁴ in neutrally stratified simulations. The size of the computational domain, nondimensionalized by the box height, is $(6 \times 5 \times 1)$, and the discretization uses $(N_x, N_y, N_z) = (144, 144, 96)$ gridpoints in the (x, y, z) directions. The neutral simulations (borrowed from Sullivan *et al.*⁴) used $(N_x, N_y, N_z) = (144, 96, 96)$ gridpoints. Considering the variation in Re_* , the grid spacing in wall units varies from 8.3 to 13.7 in the x direction and 6.9 to 11.4 in the y direction. Grid clustering near the wavy lower surface and upper boundary is used in the vertical z direction with the first u -gridpoint located in the range 0.38 to 0.63 wall units (depending on Ri). At the center of the channel, the vertical spacing is always less than 6.9 wall units. These grid spacings are chosen to capture the viscous dissipation range and are generally in accordance with other DNS.²⁶ Expressed in terms of the wave number k of the imposed surface wave, the computational box size is $(12 \times 10 \times 2)\pi$ with horizontal spacings $(k\Delta x, k\Delta y) = (0.26, 0.22)$ and a vertical spacing $k\Delta z$ varying from 0.005 near the wall to about 0.17 at the channel centerline.

Our choice of computational domain size, Reynolds number, stratification, and waveslope are a compromise between the competing requirements to have minimal disturbances from the wavy lower surface in the upper half of the channel and still retain wave influences at finite Reynolds

number. The selected parameters were found acceptable in our previous study of neutrally stratified flow. The proximity of the upper boundary is nevertheless of concern and to check on its influence we consider a higher resolution simulation $(N_x, N_y, N_z) = (240, 240, 96)$ with $Re = 16\,000$, $c = 0.125$, neutral stratification, and wave amplitude equal to half that considered above (i.e., $a = 0.008$ as opposed to $a = 0.016$). With this choice of parameters, the Reynolds number based on the wavelength remains constant. To make the higher Re simulation reasonable in terms of computational time (a factor of 8 increase is needed compared to the lower Re simulations) a smaller computational domain $(5 \times 3 \times 1)$ is used. Given the unavoidable differences in the simulation parameters (its not possible to keep ak and Re_λ constant and vary a without changing Re), we find that the results for the suite of parameters used are not strongly influenced by the proximity of the upper boundary (see the discussion of the stress in Sec. V).

All simulations are started from a linear profile in z for the mean horizontal velocity with zero initial perturbations for the velocity fields. Turbulence is triggered by small random perturbations in the temperature field. The simulations of stable stratification are spawned from well developed neutral cases. All the simulations are integrated for more than 20 000 time steps which is at least 300 large-scale (tU_o/h) time units. A typical runtime for a simulation is about 800 CPU hours on an IBM SP using 24 processors. A summary of the simulations is presented in Table I. Values of nondimensional friction velocity u_* and heat transfer q_* are obtained from averaging time series of the mean profile gradients at the top of the domain, and they are equivalent for all heights. The form stress D_p is similarly obtained by integrating the surface pressure field weighted by the surface slope gradient, according to Eq. (4).

V. RESULTS

The majority of our statistics (e.g., vertical profiles of means, variances, and wave-induced fields) are obtained by a combination of spatial and temporal averaging using more than 100 3D data volumes. To identify wave-turbulence interactions we employ both ensemble and “phase” averages. In our analysis, an arbitrary signal f is decomposed as

$$f(x, y, z, t) = \langle f(z) \rangle + f_w(x, z) + f'(x, y, z, t), \quad (3)$$

where $\langle f(z) \rangle$ is the ensemble (mean) average, $f_w(x, z)$ is the phase average, and f' are turbulent fluctuations. $\langle f \rangle$ is an average over all (x, y, t) , while f_w is the average deviation at a point (x, z) from the from mean, i.e., $f_w = \int_t \int_y \int_x f dy dt - \int_t \int_y \int_x \langle f \rangle dx dy dt$. Then $\int_t \int_y \int_x f_w dx dy dt = 0$ by construction. Further details about the averaging methods are described in Sullivan *et al.*⁴

A. Flat stationary boundary with stratification

For reference, we first show the influence of stratification on the vertical profiles of mean horizontal velocity and temperature over the entire vertical domain for a flat stationary lower boundary (Fig. 2). As expected, the mean profiles become increasingly well-mixed (in the vertical) as the level

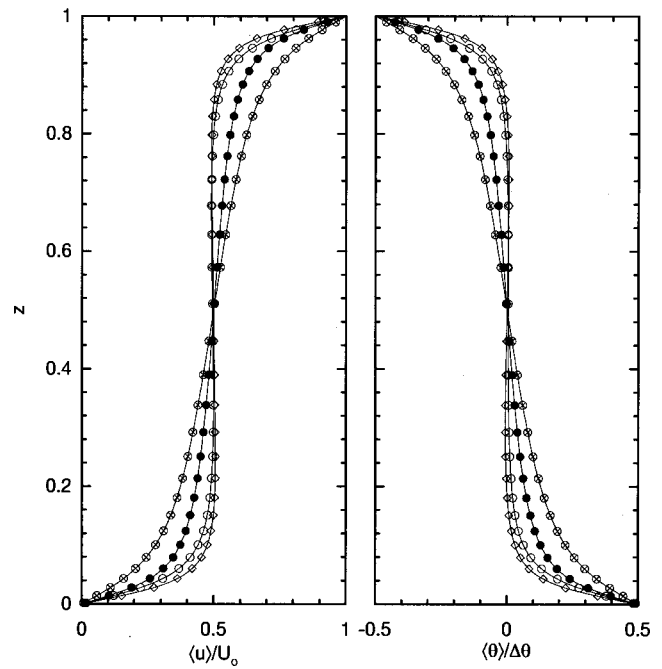


FIG. 2. Profiles of normalized mean horizontal velocity and temperature for varying Richardson numbers over a flat boundary: $Ri = -0.094$ \diamond ; -0.031 \circ ; 0 \bullet ; and 0.031 \otimes .

of stratification becomes more unstable. Notice the rapid transition to a well-mixed vertical profile even with the addition of a small amount of buoyancy (cf., cases $(0, -0.031, \text{ and } -0.094)$). Our profiles are symmetrical about the mid-plane $z = 0.5$ as required for Couette flow, and the symmetry of the profiles is an indication that the computations have reached a statistically steady state.

The combination of shear and stratification also has a significant impact on the vertical distribution and level of turbulence (Fig. 3). Here u_*^2 and $\theta_* = -q_*/u_*$ are used to normalize the velocity and temperature variances. In the middle of the domain, all four variances exhibit monotonic behavior as the stratification varies from stable to unstable; normalized $(\langle u'^2 \rangle, \langle v'^2 \rangle, \langle \theta'^2 \rangle)$ all decrease while $\langle w'^2 \rangle$ increases. Near the wall a different trend is observed; $\langle w'^2 \rangle$ changes little, $(\langle u'^2 \rangle, \langle \theta'^2 \rangle)$ show 30% increases, and $\langle v'^2 \rangle$ changes by more than a factor of 2 as Ri decreases. Qualitatively, the variance profiles at the modest value of $Ri = -0.094$ are more typical of windless Rayleigh–Bénard convection ($Ri = -\infty$) than of neutrally stratified shear flow ($Ri = 0$). The vertical profiles of v and w variances result from longitudinal roll cells that occur in our solutions at $Ri = -0.094$. Large-scale coherent structures are a persistent feature of neutral Couette flow²⁵ but our results indicate a dependence on stratification; they are enhanced with unstable stratification and disappear in stable stratification. Kommihaho *et al.*²⁵ also note a sensitivity to system rotation. Similar coherent structures have also been found in some larger-scale rotationally influenced geophysical flows like the planetary boundary layer.^{27–29} For the range of Ri considered, the shape of the variance profiles depends uniquely on the combination of shear and stratification, and thus neither u_* nor the convective velocity scale³⁰ $w_* = (gq_*h/\theta_o)^{1/3}$

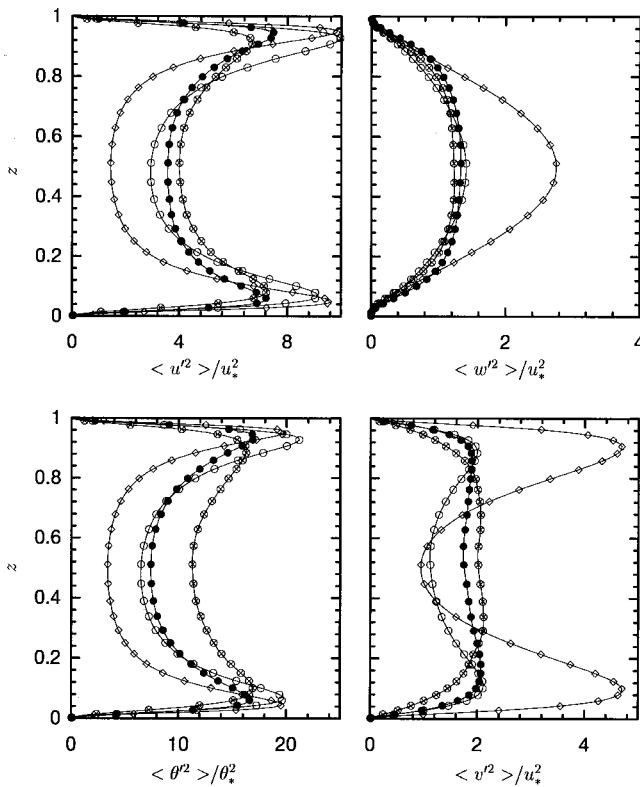


FIG. 3. Profiles of horizontal and vertical velocity variance for varying Richardson numbers. Symbols and conditions are identical to those in Fig. 2.

fully collapses the horizontal variance profiles. In LES of the planetary boundary layer, Deardorff³⁰ also reported that significantly lower (more negative) values of Ri are needed so that the turbulence intensity scales with w_*^2 . The conclusion from these results is that for the values of Ri considered thermal stratification is important and modifies the mean profiles and turbulence statistics when the upper and lower boundaries of the physical domain are flat and smooth, but the influence of the mean shear remains important.

B. Mean and variance profiles over a moving wavy boundary

Vertical profiles of average horizontal velocity and temperature in terms of wall variables are depicted in Figs. 4 and

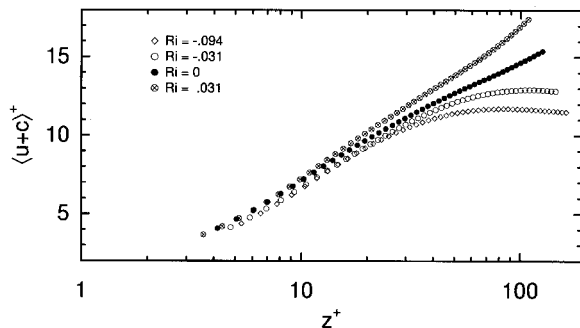


FIG. 4. Vertical profile of mean horizontal velocity in wall units for stratified shear flow over a wavy boundary with $c/U_c=0.5$ for varying Ri. Here $U_c=U_o/2$ is the channel centerline velocity.

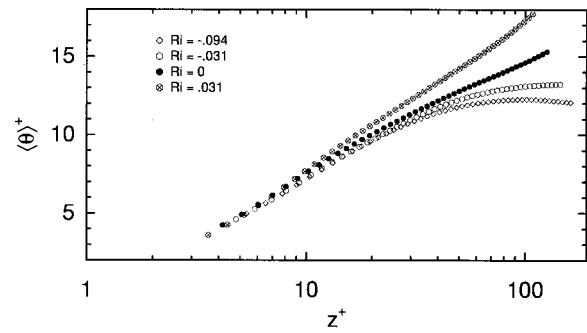


FIG. 5. Vertical profile of mean temperature $\langle \theta \rangle^+ = \langle (\theta - \theta_L) / \theta_* \rangle$ for stratified shear flow over a wavy boundary with $c/U_c=0.5$ for varying Ri.

5, respectively, for a moving wave with $c/U_c=0.5$ ($U_c=U_o/2$ is the velocity at the channel centerline). Waves with $c \approx 0.25$ and less are of particular interest since wave growth typically occurs in this regime (see Sec. V). The mean profiles of (u, θ) , shown in Figs. 4 and 5, are obtained by first interpolating the instantaneous velocity and temperature fields in wave following coordinates to a flat stationary coordinate system and then averaging in horizontal $(x-y)$ planes and in time; the flat coordinate system begins just above the wave crests.⁴ Wall variables for velocity, temperature, and length are defined as $(u^+, \theta^+, z^+) = (u/u_*, (\theta - \theta_L)/\theta_*, z u_* / \nu)$. The profiles of velocity and temperature over moving waves exhibit the same overall trends as the flat stationary boundary case; as the stratification varies from unstable to stable the extent over which the profiles maintain a significant vertical gradient increases. In wall variables, the profiles of velocity and temperature with stable (unstable) stratification lie above (below) those for the neutral case. This is caused by the decreased (increased) turbulence levels in stable (unstable) stratification which is reflected in the variation of (u_*, q_*) shown in Fig. 6. The mean profiles for the stratifications considered nearly collapse below $z^+ < 10$, which is expected from Monin–Obukhov similarity theory.³¹ The latter accounts for stratification in the surface layer of the planetary boundary layers and predicts that buoyancy influences dominate when z is greater than the Monin–Obukhov length $L = -u_*^3 / g \beta \kappa q_*$ (here κ is the von-Kármán constant and β is the coefficient of thermal expansion). At $z^+ > 10$, the profiles gradually depart with the stable (unstable) profiles exhibiting higher (lower) values of normalized velocity and temperature compared to the strictly log-linear variation. This is also in qualitative agreement with Monin–Obukhov similarity theory. Far away from the wavy boundary the velocity and temperature profiles approach the centerline in a slightly nonmonotonic manner. This behavior is due to the longitudinal roll system present at $Ri = -0.094$ mentioned previously. Additional computations (not shown) at even more negative values of Ri show a similar trend in the mean profiles while calculations at $Ri = -\infty$ (i.e., free convection) do not display this behavior.

It is also interesting to note that the variation of friction velocity and heat flux in Fig. 6 for a given wave age is much less than the variability with stratification. In addition, we find that $q_* = u_*^2$ to a good approximation. This is in agree-

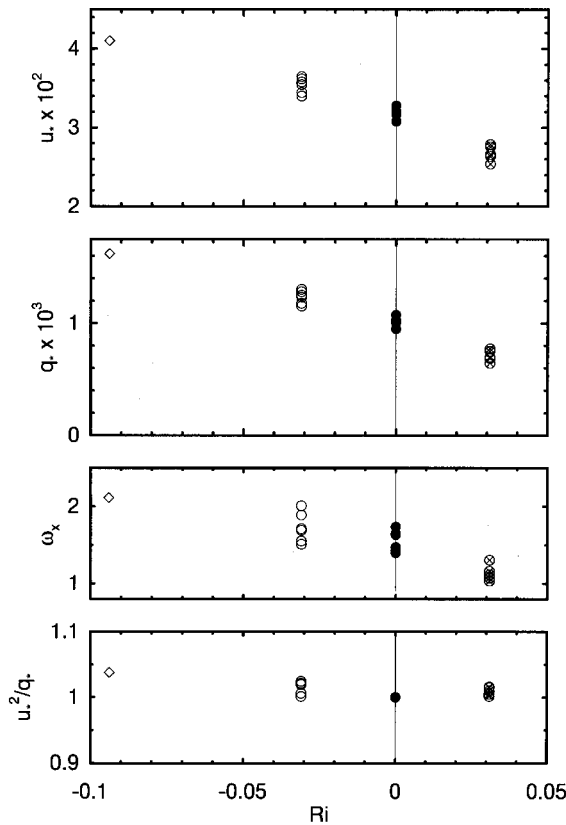


FIG. 6. Variation of normalized friction velocity (u_*), heat flux (q_*), streamwise vorticity intensity (ω'_x), and flux ratio (u_*^2/q_*) as function of bulk Richardson number. The cluster of points at each Ri depict the variation with wave age. ω'_x was computed at $z=0.06$ (or $kz=0.37$) from the lower boundary.

ment with Reynolds analogy,³² which in its simplest form states that the momentum and heat transfer are equal for laminar, incompressible flow with $Pr=1$. Since q_* and u_*^2 are constant with height in Couette flow our results imply that the turbulent Prandtl number in our flow is near unity. The streamwise vorticity intensity, $\omega'_x = \langle (\partial w / \partial y - \partial v / \partial z)^2 \rangle^{1/2}$, near the lower boundary is observed to increase with decreasing stratification with a slight variation with wave age. We take ω'_x as a measure of the strength of streamwise roll cells, and the observed variation suggests that they strengthen as the stratification becomes more unstable over the range of Ri considered. The presence of low amplitude moving waves only slightly alters their formation and strength. Calhoun and Street¹⁵ using the λ_2 -method³³ also find streamwise vortices on the upwind face of stationary topography.

The velocity and temperature variances above moving waves in the presence of stratification are depicted in Fig. 7. Compared to the flat bottom cases (Fig. 3), the presence of a moving wavy boundary has altered the vertical profiles of the u and θ variances to the greatest extent. In the flat coordinate system used for analysis here, the maximum u variance occurs just above the wave crests and with a slightly reduced amplitude (about 10 to 15%) when $Ri = -0.094$. The maximum θ variance is also just above the tops of the waves but with a larger reduction in the amplitude as much as 40%. The

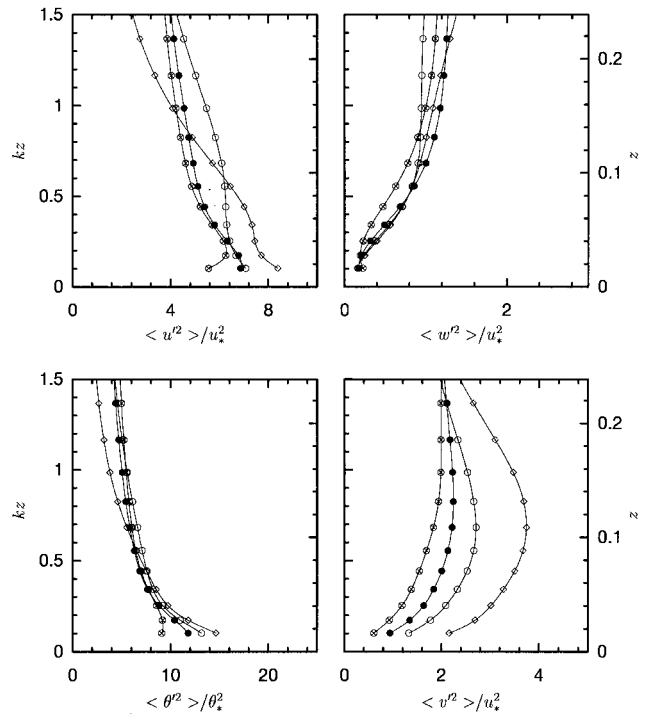


FIG. 7. Variation of velocity and temperature variances at wave speed $c/U_c=0.5$, symbols and conditions as in Fig. 5. The vertical axis along the left and right side of each plot is in units of kz and z , respectively.

shape and magnitude of the w and v velocity variances exhibit the same behavior as in the flat bottom case; the w variance is almost independent of stratification, while the v variance is greatest with the most unstable stratification. In Sullivan *et al.*,⁴ we also reported that for neutrally stratified flow, slow-moving waves reduced the u variance slightly with only small increases in the w variance. It is not surprising that the v variance is not altered appreciably since our waves are two-dimensional (no y variation) and of modest slope, $ak=0.1$, with no significant flow separation. Flow separation over a stationary wave can cause the detached shear layer to impact the windward face of the downstream wave, leading to vigorous oscillations in v .^{14,15,34,35} The oscillations in v might further be excited by the presence of streamwise (Görtler vortices).¹⁵ The parameter space investigated by these studies is outside the present regime since they consider steep stationary waves with $0.157 < ak < 0.628$.

C. Form stress and wave growth

One of the important questions to consider is the influence of stratification on the surface pressure field and hence its role for wave growth. In Fig. 8, we show the variation of form stress (normalized by U_o^2)

$$D_p = \frac{1}{\lambda} \int_0^\lambda p \frac{dz_b dy}{dx} dx, \tag{4}$$

as function of wave phase speed with the Richardson number as a parameter. Here $dz_b dy/dx$ is the slope of the underlying waveform. In general, the surface drag is higher (lower) for unstable (stable) stratification compared to the neutral case,

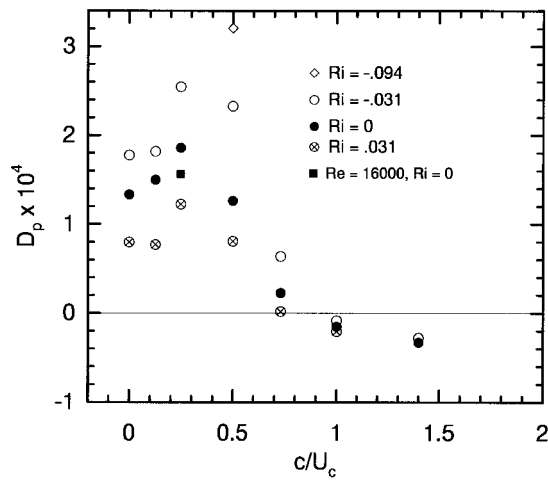


FIG. 8. Surface form stress for several values of c/U_c with varying Ri.

but with a dependence on the wave speed. A similar trend was also observed by Voorrips *et al.*⁹ Large changes in form stress are obtained at low values of c ; e.g., at $c=0.5$, the drag varies by more than a factor of 3 as Ri varies from -0.094 to 0.031 . Fast-moving waves, for which the form stress is near zero or slightly negative, are least influenced by the changes in the stratification. In field measurements, both the friction velocity u_* and U_{10} (the velocity at 10 m) have frequently been used to scale the wave growth. Kahma and Calhoun¹⁰ were unable to settle the question as to which scale velocity is more appropriate, partly because true u_* is often not available from field measurements (empirical laws frequently are used to estimate surface drag from other observations). In Fig. 9, we have re-plotted the results from Fig. 8 using nondimensional coordinates ($D_p/u_*^2, c/u_*$). For the ideal cases considered here (i.e., a single monochromatic wave), the primary effects of unstable, neutral, and stable stratification are accounted for by employing u_* scaling for both the drag and wave age. Close inspection of our results in Fig. 9 suggest that at low wave age there is a persistent trend for the normalized drag to be higher with increasing unstable stratification. This is in agreement with

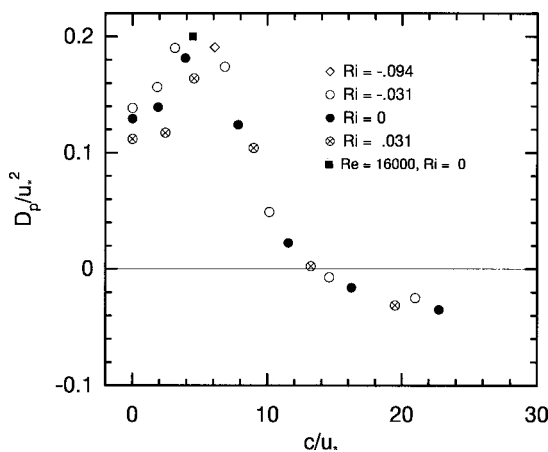


FIG. 9. Surface form stress, normalized by u_*^2 , for several values of wave age c/u_* with varying Ri.

the second-order closure model of Voorrips *et al.*⁹ However, their model predictions also show that this same trend continues for fast-moving waves, which is not supported by the present calculations. Fast-moving waves carry little form stress, hence it is difficult to resolve the influence of stratification from the statistical variability in the drag. Voorrips *et al.*⁹ did not consider the regime where the waves are moving faster than the winds with stratification. The latter is an intriguing regime since the pressure transport from waves to the atmosphere can produce a wave-driven wind increase.³⁶

Note that the nondimensional form stress in Fig. 9 from the higher Re simulation with $a=0.008$ is in close agreement with the trend from the lower Re simulations with $a=0.016$. This provides evidence that the lower Re simulations with larger wave amplitude are not strongly contaminated by the presence of the upper boundary. The slightly elevated drag obtained at $Re=16000$ is likely due to the smaller horizontal domain used in this simulation. Kommihaho *et al.*²⁵ show that in Couette flow the turbulence intensity increases with decreasing horizontal domain size which supports our premise that higher levels of turbulence lead to increase form stress.

The determination of drag, and hence wave growth, from measurements is a challenging task as knowledge of the surface pressure field is generally unknown. Typically, the surface pressure field is inferred from measurements taken slightly above the water surface and extrapolated downward using a potential flow assumption. Plant³⁷ synthesized a large body of the existing data and reported measurements of the fractional rate of energy transfer to the wave field, β . For a deep-water wave, the fractional rate of energy transfer is related to the form stress via^{38,39}

$$\beta = \frac{1}{\omega E} \frac{dE}{dt} = 2 \frac{\rho}{\rho_w} \frac{D_p}{(ak)^2} \left[\frac{u_*}{c} \right]^2, \tag{5}$$

where the energy of the wave is $E = \rho_w g a^2 / 2$, wave frequency is $\omega = ck$, the density ratio of air-to-water is ρ / ρ_w , and ak is the wavenumber. In the above, we neglect the contribution from the surface shear stress⁴⁰ and evaluate the form stress D_p using the pressure field at a smooth water surface $z = z_{bdy}$. In Eq. (5), β only accounts for the wave growth induced by the wind field. (Wave growth can also be induced by nonlinear wave-wave interactions in a sea with a multi-component wave spectrum.⁴¹) In Fig. 10, the wave growth deduced from our simulations is compared to measurements [using Eq. (5) with $\rho / \rho_w = 1.25 \times 10^{-3}$]. In making this comparison it is important to keep in mind the modeling assumptions used. The DNS is performed at low-Re, in a finite depth domain, and the underlying surface is assumed to be a smooth, monochromatic wave with no time evolution. We have some evidence that the finite domain is not significantly influencing the results but the other assumptions can only be addressed by considering LES or DNS with higher Re and a more realistic wavy surface. Reasonable quantitative agreement is observed despite the modeling restrictions and the uncertainties in the measurements. The scatter in the data emphasizes the difficulty of making wave-growth measurements in both the field and wind-wave tanks. In this

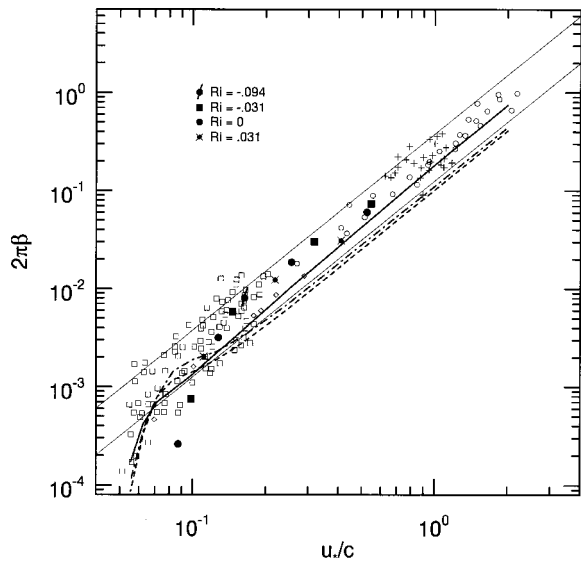


FIG. 10. The fractional rate of energy transfer to the waves due to pressure drag as function of inverse wave age. Light symbols are measurements synthesized by Plant (1982), and dark symbols are results from present DNS with varying Ri. The thin solid lines are obtained from the empirical formula $\beta = (0.04 \pm 0.020)(u_*/c)^2$. Results from rough-wall, second-order closure models are from Li (1995) and Li *et al.* (2000): $E-kz$ closure (thick solid line), q^2-l closure (dashed-dotted line), and Launder-Reece-Rodi (closure dashed line).

figure, we also include estimates of wave growth from three different rough-wall second-order closure models.^{38,39} These calculations assume a monochromatic wave field with $ak = 0.1$ and a uniform surface roughness of $z_o = 0.0001$ m. In general, the predictions from our low-Re DNS agree better with the measured wave growth for $u_*/c > 0.1$ (or $c/u_* < 10$) than do estimates from the much higher-Re closure models.

Predictions from second-order closure with finite Reynolds number show an increase in form stress with decreasing Re ^{42,43} and thus Re effects is a possible explanation for the discrepancies between model predictions and measured wave growth. Also, Harris *et al.*⁴³ point out that the roughness Reynolds number for oceanic conditions is frequently in the transitional regime, and thus the turbulent flow is likely Reynolds-number dependent. One consequence of the low-Re in our simulations is the early transition in the sign of the form stress (i.e., the point where the flow switches from wind-driven waves to wave-driven winds). This transition occurs near $c/u_* \approx 14$ (see Fig. 9) whereas high-Re, rough-wall, second-order closure predicts a transition near $c/u_* \approx 22$. This Reynolds-number effect also manifests itself in Fig. 10 at low values of inverse wave age ($u_*/c < 0.1$) where the DNS predictions depart from the measurements. However, if measured wave-growth data were presented as a function of the wave age c/u_λ , where u_λ is the mean wind speed at one wavelength above the surface, then the transition from wind-driven waves to wave-driven winds is relatively independent of Reynolds number.⁴ However, u_λ is not routinely reported in most field observations.

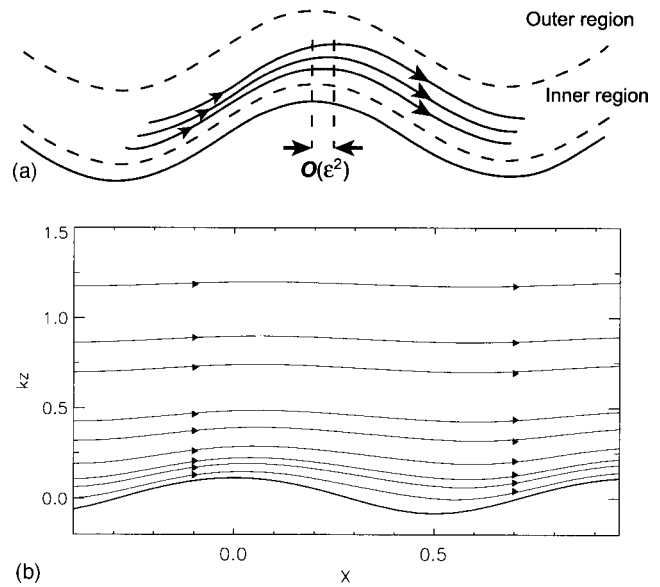


FIG. 11. Neutrally stratified flow over low-amplitude stationary topography illustrating the nonseparated sheltering mechanism. (a) Sketch of streamline pattern from Belcher and Hunt (Ref. 3). $\epsilon = u_*/U_o$ where u_* is the friction velocity and U_o is a mean velocity scale in the approach flow. (b) Average streamlines computed from DNS of Sullivan *et al.* (Ref. 4).

D. Phase-average pressure and velocity fields

One of the primary conclusions of Belcher and Hunt³ is that the highly turbulent flow near the surface of a hill produces an asymmetrical pattern of mean flow streamlines as shown in Fig. 11. They identify this nonseparated sheltering mechanism as the dominant contributor to the form stress. Streamlines from our DNS of neutrally stratified, stationary-wave flow⁴ shown in Fig. 11 are in agreement with those sketched by Belcher and Hunt. An important question is then how is this flow pattern altered by moving waves? In Fig. 12, phase-average streamline patterns over moving waves at constant $c = 0.25$ for varying Richardson number are depicted along with the height of the critical layer, i.e., the vertical location z_{cr} where the average streamwise velocity $\langle u \rangle + u_w = c$. First, we note that the streamlines are strongly asymmetrical about the wave crest and are modified compared to those shown in Fig. 11 by the orbital velocities of the water and the presence of a critical layer. Blocking by the critical layer displaces the streamlines downwind of the crest and appears to enhance the nonseparated sheltering mechanism (also see Belcher and Hunt¹). Both the streamline patterns and z_{cr} are strong functions of the stratification. At the most negative Ri considered, z_{cr} lies very near the wave surface especially just upstream of the wave crest. With increasing Ri, z_{cr} becomes elevated, and the region of closed streamlines broadens. The vertical variation of z_{cr} with stratification is expected, since for a given c , z_{cr} increases (decreases) as u_* decreases (increases), according to a neutral log-law argument, i.e., $c \approx (u_*/\kappa) \ln z_{cr}^+ + B$. The compactness of the streamline patterns and the proximity of the critical-layer height to the surface correlate with the form stress; i.e., as z_{cr} decreases D_p increases. This trend continues until the critical layer becomes totally immersed in the

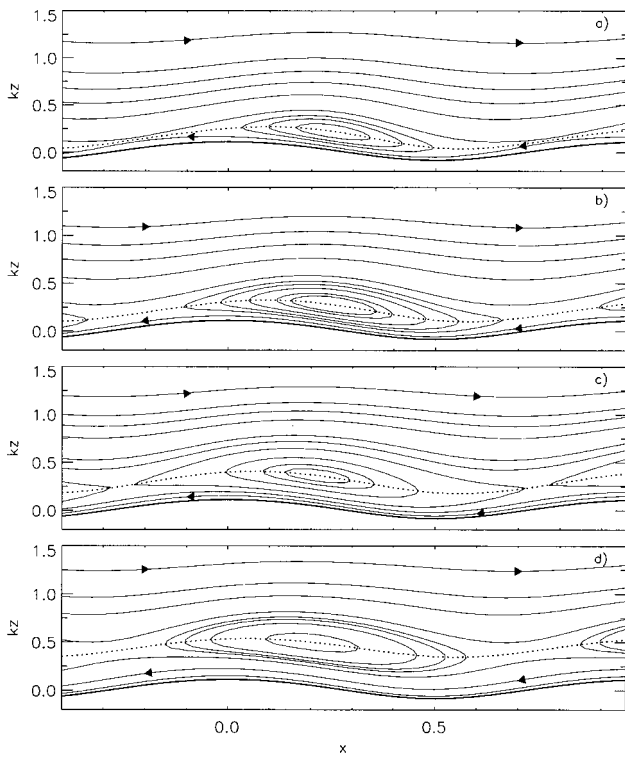


FIG. 12. Average streamline pattern at constant wave phase speed $c/U_c = 0.5$ showing the variation of the critical layer with $Ri = (-0.094, -0.031, 0, 0.031)$, panels (a)–(d), respectively. The height of the critical layer is indicated by a dotted line.

viscous sublayer, and then the drag begins to approach the value for stationary waves. The variation of the average critical-layer height, $\langle z_{cr} \rangle = \int_x z_{cr} dx / \lambda$, with stratification is displayed in Fig. 13. As a function of wave age c/u_* the

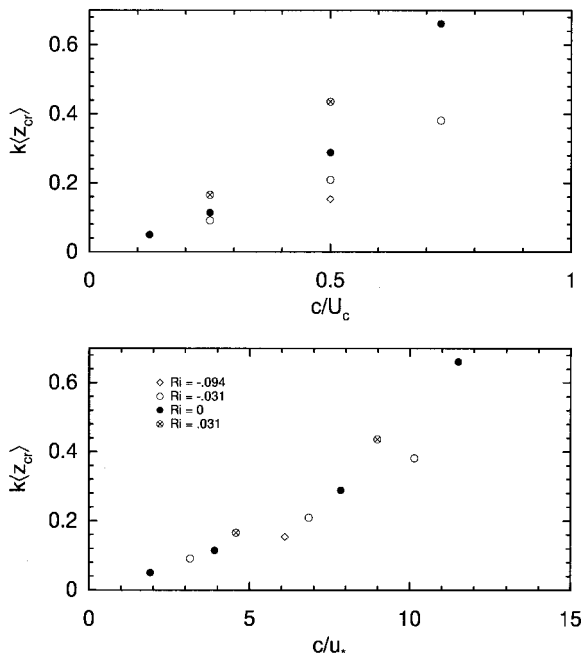


FIG. 13. Variation of the average critical layer height with constant wave speed (upper panel) and wave age c/u_* (lower panel) for unstable, neutral, and stable stratifications.

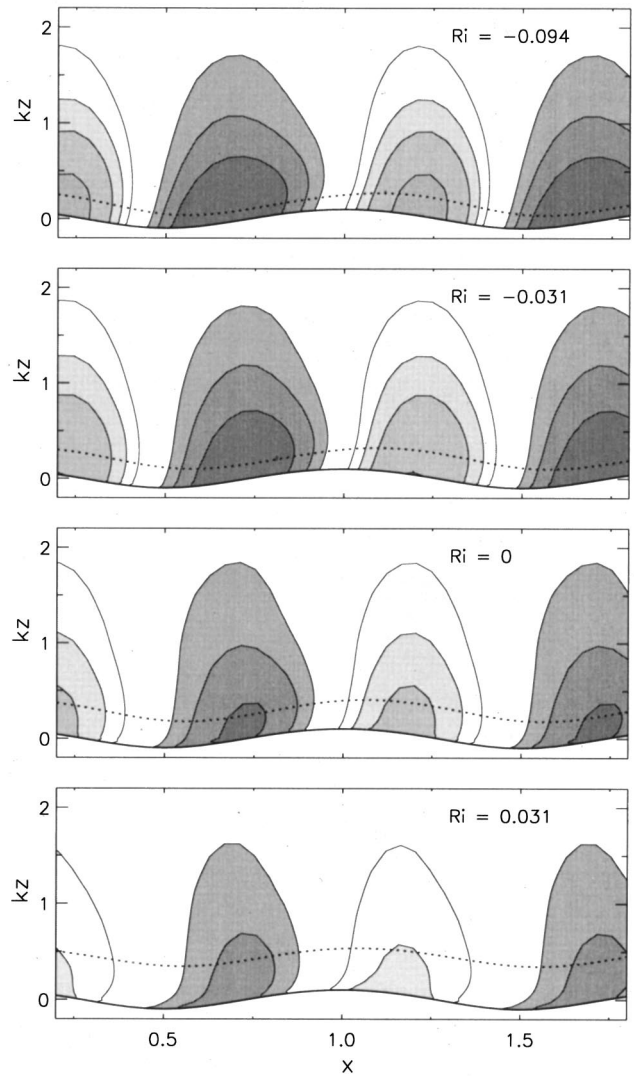


FIG. 14. The wave-correlated pressure field, $p/\rho u_*^2$, at $c=0.25$ for varying stratification. The contour values, within each family of contours, are darker to lighter with negative values ($-4.0, -2.4, -1.6, -0.9$) for the light shaded family, and complementary positive values for the dark shaded family. The critical level is indicated by a dotted line.

results reasonably collapse for the range of stratifications considered. Thus we conclude that the primary influence of stratification on the critical-layer height is to alter the turbulence intensity level, which can be largely accounted for through the nondimensional wave age c/u_* .

The phase-average p_w/u_*^2 field (see Fig. 14) shows how the vertical pressure field contributes to the form stress. Regions of positive and negative pressure contours form asymmetrically on the upwind and downwind slopes in accordance with non-separated sheltering. Near z_{cr} , the contours are distorted by critical layer dynamics, but become vertically uniform as $z \gg z_{cr}$. The strength of the pressure field increases with unstable stratification while the near-surface centroid of the pressure contours remains nearly constant. For faster moving waves, nearly symmetrical negative (positive) pressure contours form over the crest (trough) of the wave (not shown).

In Figs. 15 and 16, the variation of the wave-induced

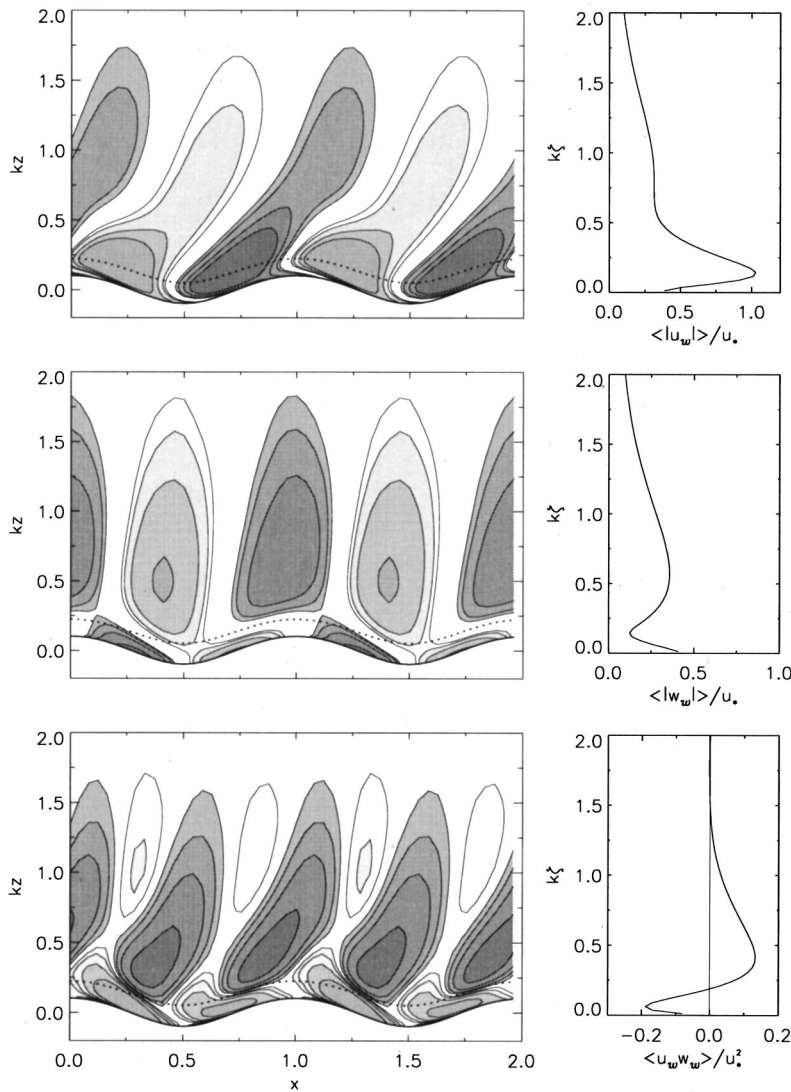


FIG. 15. Phase averaged fields $(u_w, w_w)/u_*$, $u_w w_w / u_*^2$ for case $(\text{Ri}, c) = (-0.094, 0.25)$. The dark (light) family of contours correspond to positive (negative) values, respectively: upper panels for u_w , contour values $(\pm 0.2, \pm 0.3, \pm 0.5, \pm 0.7)$, magnitude of wave integrated u_w is shown on the right; middle panels for w_w , with contour values $(\pm 0.15, \pm 0.2, \pm 0.3, \pm 0.5)$; lower panels for flux $u_w w_w$, contour values $(\pm 0.02, \pm 0.05, \pm 0.1, \pm 0.2)$. The dotted line is the critical layer height where $\langle u \rangle + u_w = 0$.

horizontal velocity u_w , vertical velocity w_w and momentum flux $u_w w_w$ are displayed for different levels of stratification and constant wave speed $c=0.25$. The presence of stratification is found to alter the shape and magnitudes of the wave-induced fields, but they remain synchronized with the positioning of the critical-layer height; z_{cr} varies by a factor of two for $\text{Ri} = [-0.094, 0.031]$ (see Fig. 13). At $\text{Ri} = -0.094$, z_{cr} lies closer to the wave surface, and the absolute magnitudes of (u_w, w_w) are larger than their counterparts with stable stratification (note the normalization by u_*). The normalized wave-induced momentum flux below the critical layer is about 20% of u_*^2 independent of stratification. Notice that in the case $\text{Ri} = -0.094$, $u_w w_w$ above the critical layer is positive and noticeably greater than in the case with stable stratification. A similar trend also happens in neutrally stratified flow as the phase speed varies from $c < 1$ to $c > 1$ and results from the “flattening” of the critical layer as z_{cr} moves away from the wall. When compared to the neutrally stratified situation, unstable stratification results in wave-induced flow fields typical of slower moving waves, while the opposite holds for stable stratification. This behavior of the flow fields is consistent with the

previous observation that scaling by u_* tends to collapse the form stress for actively growing waves in the presence of stratification.

E. Wave-induced temperature field

We next analyze the temperature fields using the same methods as for velocity in order to examine the impact of wave-induced motions for scalar transport. Scalar transport is typically ignored in most theoretical models of turbulent flow over wavy surfaces because of their focus on neutrally stratified flow. The wave-induced component θ_w is shown in Figs. 17 along with w_w and the wave-induced heat flux $\theta_w w_w$ for unstable stratification. θ_w is a significant contributor to the temperature field, and the θ_w contours further show that the wave-induced temperature field is clearly organized by the motion of the waves. Near the surface, concentrations of positive and negative temperatures patches are found at the crest and trough. These patches are tilted downwind as z increases because of the mean wind, a trend more evident in the case with unstable stratification. This organization of the

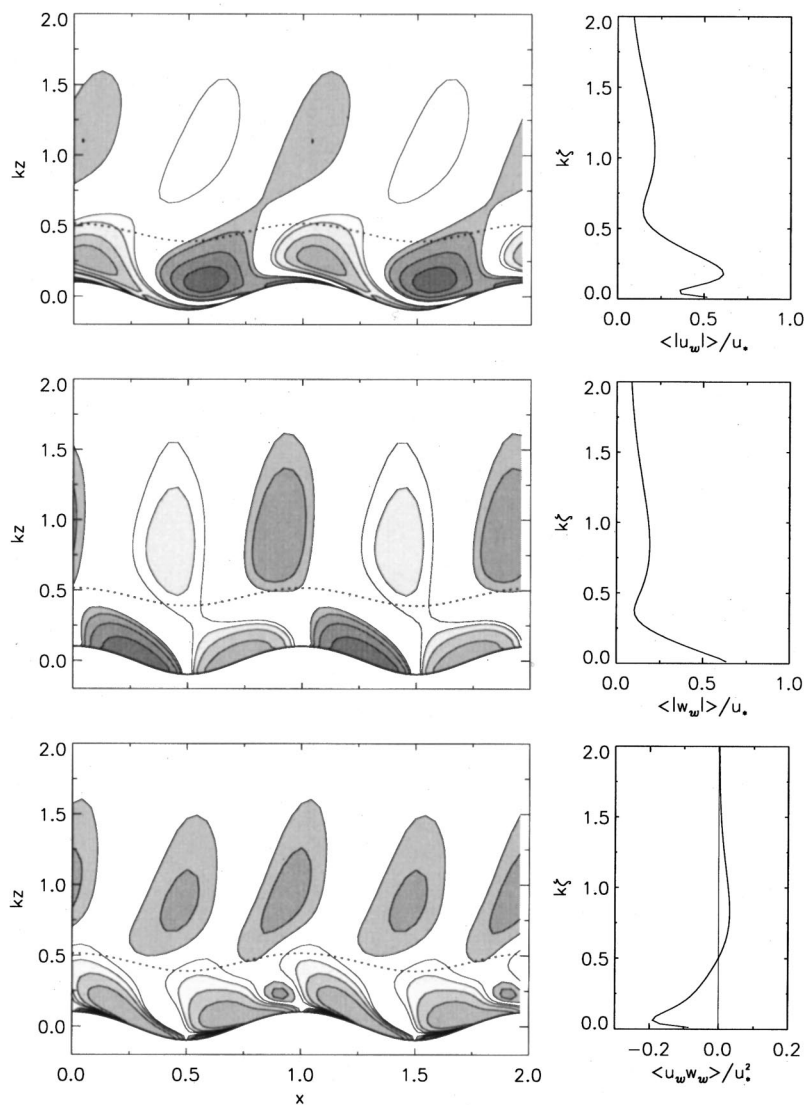


FIG. 16. Phase averaged fields for $(\text{Ri}, c) = (0.031, 0.25)$ in surface following coordinates. The variables and contouring scheme are the same as in Fig. 15.

temperature field can be interpreted using the contour plots of the wave-induced velocity fields in Fig. 15. At the wave crest, there is convergence of the horizontal wave-induced flow field accompanied by rising vertical velocity motion. An opposite pattern happens in the trough; horizontal divergence with sinking vertical motion. As a result of the coherence in u_w and w_w , warmer air near the surface is focused at the crest from both windward and leeward sides and is then transported upward by the vertical velocity. Similarly, at the wave trough cooler air is transported downward because of the horizontal divergence. A similar pattern, but with opposite signs in the temperature field, also occurs for stable stratification; cool and warm air are now focused over the crest and trough, respectively.

The mechanism we propose for the organization of the temperature field in flow over waves is closely linked to the presence of a wave induced velocity field. This differs from windless Rayleigh-Bénard convection over stationary wavy terrain^{19,20} where a coherent temperature field was only observed for certain combinations of surface wavelength and domain height (see also McWilliams *et al.*⁴⁴). Our proposed

mechanism is active whenever a mean wind and wave field are present.

The resulting pattern for θ_w leads to a complex parameter dependence of the wave-induced heat flux. In the $\text{Ri} = -0.031$ case, $\theta_w w_w$ can be as much as 15% of the surface heat flux near the surface. However, the wave-induced heat flux changes sign above the critical layer because of the horizontal phase shift in the wave-induced vertical velocity. In the case with stable stratification, $\theta_w w_w$ is weaker because now w_w is primarily induced on the leeward side of the waves, and w_w above z_{cr} is considerably less than in the case with unstable stratification.

VI. CONCLUSIONS

We find that for the range of stability conditions considered, stratification most influences the regime of actively growing waves, i.e., waves with phase speed $c < 1$. The increased (decreased) turbulence levels present with unstable (stable) stratification lead to higher (lower) friction velocity u_* . As a result, the form stress variation with wave age

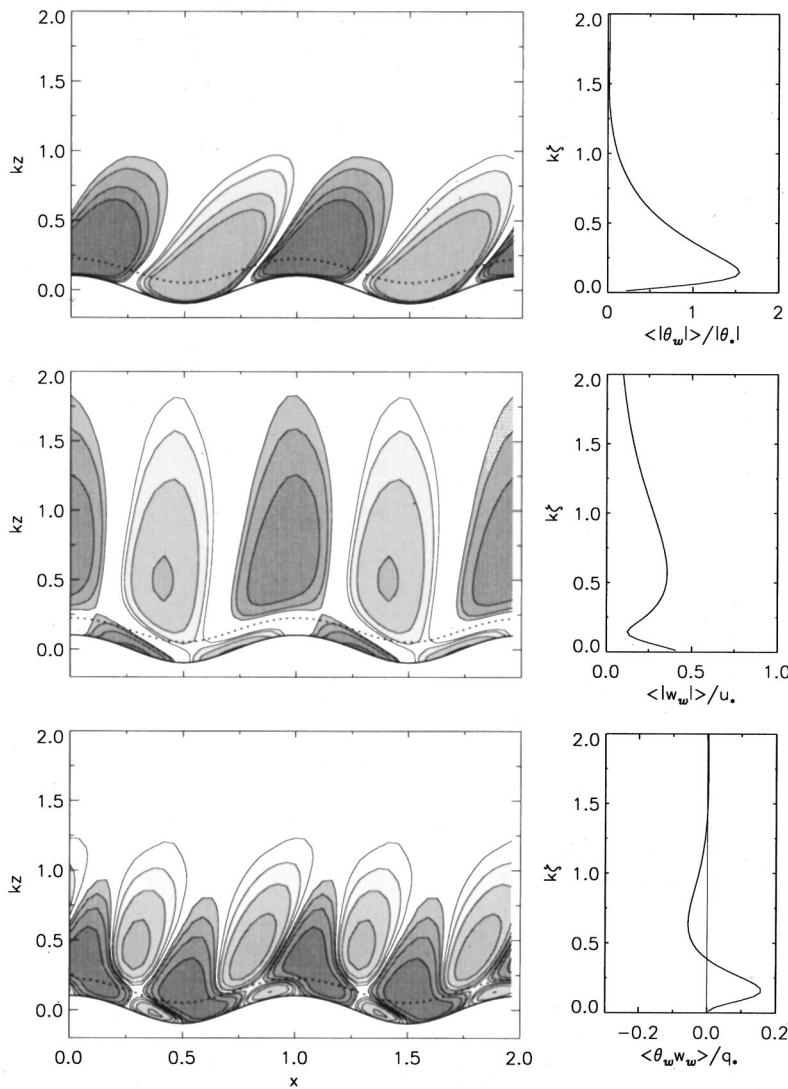


FIG. 17. Phase averaged fields $\theta_w/|\theta_*|$, w_w/u_* , $\theta_w w_w/q_*$ for $(Ri,c)=(-0.094,0.25)$. The shading scheme is identical to Fig. 15: upper panels for θ_w , contour values ($\pm 0.2, \pm 0.3, \pm 0.5, \pm 0.7$); middle panels for w_w , with contour values ($\pm 0.15, \pm 0.2, \pm 0.3, \pm 0.5$); lower panels for flux $\theta_w w_w$, contour values ($\pm 0.02, \pm 0.05, \pm 0.1, \pm 0.2$). The dotted line is the critical layer height.

collapses reasonably well when the drag is normalized by u_*^2 and wave age is expressed as c/u_* . The nonseparated sheltering mechanism,¹ dominate in neutral hill flow, is modified by stratification, movement of the underlying wavy surface, and the close proximity of a critical layer. Despite the disparity in Re, the DNS predictions of wave growth are in reasonable agreement with measured values obtained from field measurements and laboratory experiments.

The near-surface flow patterns and in particular the critical-layer height variation are well correlated with the level of stratification. As the bulk Richardson number varies from negative to positive values (unstable to stable stratification), the critical-layer height z_{cr} increases in accordance with the decreasing turbulence levels (or lower values of u_*). Wave induced velocity, vertical momentum, temperature, and heat flux are also found to be strong functions of the stratification level. Compared to the situation of neutral stratification, the phase-average flow patterns with unstable stratification are similar to the flow patterns over slower moving waves while stable stratification induces flow patterns typical of faster moving waves. The wave-induced temperature field responds in an organized manner to the wave-

induced velocity field. In the situation of unstable stratification, positive and negative temperature patches form over the wave crests and troughs, respectively. A similar pattern holds for the case of stable stratification but with cool and warm air now concentrated over the wave crests and troughs, respectively. The variation of the wave-induced temperature field results from the convergence and divergence of the phase-average velocity fields. The wave induced momentum flux can be as much as 15% of the total surface heat flux. For a waveslope $ak=0.1$, no evidence of flow separation is observed in the instantaneous or phase average flowfields over the range of stabilities considered.

The present results, although obtained at low DNS Reynolds numbers, have implications for higher Reynolds number flows. Field measurements are needed close to a wavy surface to find evidence of critical-layer dynamics and to obtain information about the correlations between wave-induced scalar and velocity fields for a range of stratifications. We propose that wave age based on either u_* or u_λ (where u_λ is the wind speed at one wavelength above the surface) is more appropriate than the commonly used wind speed at 10 m. The present results with and without waves

are in qualitative agreement with Monin–Obukhov similarity theory but they do not reproduce the similarity functions³¹

$$\phi_m = \frac{\kappa z}{u_*} \frac{\partial u}{\partial z} \equiv \kappa z^+ \frac{\partial u^+}{\partial z^+}, \quad \phi_\theta = \frac{\kappa z}{\theta_*} \frac{\partial \theta}{\partial z} \equiv \kappa z^+ \frac{\partial \theta^+}{\partial z^+}, \quad (6)$$

in the flat bottom case to sufficient accuracy to warrant making quantitative statements about the influence of waves on (ϕ_m, ϕ_θ) in field observations. Given the departures we see from classical Monin–Obukhov similarity theory we speculate that the presence of large-scale coherent structures interfere with the Monin–Obukhov assumptions that the only controlling length scale, outside the viscous sublayer, is the distance from the boundary. Recent LES and observations^{29,45} also suggest a dependence of Monin–Obukhov similarity theory on the depth of the atmospheric boundary layer. However, further investigation at even higher Reynolds number are needed to assess this hypothesis. It would be of particular interest to obtain measurements and perform computations for very fast moving waves under conditions of stratification where deviations from Monin–Obukhov similarity theory are potentially important.

ACKNOWLEDGMENTS

We are grateful to Peter Taylor for several discussions and for supplying us with the experimental data and second-order closure results in Fig. 10. Edward Patton and the anonymous reviewers provided constructive comments in the preparation of the manuscript. NCAR is sponsored by the National Science Foundation. A part of this work was supported by the Office of Naval Research through the CBLAST initiative, Contract No. N00014-00-C-0180.

- ¹S.E. Belcher and J.C.R. Hunt, “Turbulent flow over hills and waves,” *Annu. Rev. Fluid Mech.* **30**, 507 (1998).
- ²S.E. Belcher, T.M.J. Newley, and J.C.R. Hunt, “The drag on an undulating surface induced by the flow of a turbulent boundary layer,” *J. Fluid Mech.* **249**, 557 (1993).
- ³S.E. Belcher and J.C.R. Hunt, “Turbulent flow over slowly moving waves,” *J. Fluid Mech.* **251**, 109 (1993).
- ⁴P.P. Sullivan, J.C. McWilliams, and C.-H. Moeng, “Simulation of turbulent flow over idealized water waves,” *J. Fluid Mech.* **404**, 47 (2000).
- ⁵S.E. Belcher, J.C.R. Hunt, and J.E. Cohen, “Turbulent flow over growing waves,” in *Wind-over-Wave Couplings: Perspectives and Prospects*, edited by S.G. Sajjadi, N.H. Thomas, and J.C.R. Hunt (Clarendon, New York, 1999), pp. 19–29.
- ⁶J.C.R. Hunt, K.J. Richards, and P.W.M. Brighton, “Stably stratified shear flow over low hills,” *Q. J. R. Meteorol. Soc.* **114**, 859 (1988).
- ⁷S.E. Belcher and N. Wood, “Form and wave drag due to stably stratified turbulent flow over low ridges,” *Q. J. R. Meteorol. Soc.* **122**, 863 (1996).
- ⁸P.A.E.M. Janssen and G.J. Komen, “Effect of atmospheric stability on the growth of surface gravity waves,” *Boundary-Layer Meteorol.* **32**, 85 (1985).
- ⁹A.C. Voorrips, V.K. Makin, and G.J. Komen, “The influence of atmospheric stratification on the growth of water waves,” *Boundary-Layer Meteorol.* **72**, 287 (1995).
- ¹⁰K.K. Kahma and C.J. Calkoen, “Reconciling discrepancies in the observed growth of wind-generated waves,” *J. Phys. Oceanogr.* **22**, 1389 (1992).
- ¹¹Y.A. Papadimitrakis, Y.-H.L. Hsu, and J. Wu, “Turbulent heat and mass transfers across a thermally stratified air-water interface,” *J. Geophys. Res.* **91**, 10 607 (1986).
- ¹²Y.A. Papadimitrakis, Y.-H.L. Hsu, and J. Wu, “Thermal stability effects on the structure of the velocity field above an air-water interface,” *J. Geophys. Res.* **92**, 8277 (1987).
- ¹³Here z^+ is the height above the mean water level expressed in wall units,

- $z^+ = zu_* / \nu$, where u_* is the friction-velocity and ν the fluid viscosity.
- ¹⁴P. Cherukat, Y. Na, T.J. Hanratty, and J.B. McLaughlin, “Direct numerical simulation of a fully developed turbulent flow over a wavy wall,” *Theor. Comput. Fluid Dyn.* **11**, 109 (1998).
- ¹⁵R.J. Calhoun and R.L. Street, “Turbulent flow over a wavy surface: Neutral case,” *J. Geophys. Res.* **106**, 9277 (2001).
- ¹⁶W. Gong, P.A. Taylor, and A. Dornbrack, “Turbulent boundary-layer flow over fixed aerodynamically rough two-dimensional sinusoidal waves,” *J. Fluid Mech.* **312**, 1 (1996).
- ¹⁷J.A. Domaradzki and R.W. Metcalfe, “Direct numerical simulations of the effects of shear on turbulent Rayleigh–Bénard convection,” *J. Fluid Mech.* **193**, 499 (1988).
- ¹⁸R.I. Sykes and D.S. Henn, “Large-eddy simulation of turbulent sheared convection,” *J. Atmos. Sci.* **46**, 1106 (1989).
- ¹⁹K. Krettenauer and U. Schumann, “Direct numerical simulation of thermal convection over a wavy surface,” *Meteorol. Atmos. Phys.* **41**, 165 (1989).
- ²⁰K. Krettenauer and U. Schumann, “Numerical simulation of turbulent convection over wavy terrain,” *J. Fluid Mech.* **237**, 261 (1992).
- ²¹Y. Zang, R.L. Street, and J.R. Koseff, “A nonstaggered grid, fractional step method for time-dependent incompressible Navier–Stokes equations in curvilinear coordinates,” *J. Comput. Phys.* **114**, 18 (1994).
- ²²C.M. Rhie and W.L. Chow, “A numerical study of the turbulent flow past an isolated airfoil with trailing edge separation,” *AIAA J.* **21**, 1525 (1983).
- ²³P.P. Sullivan, J.C. McWilliams, and C.-H. Moeng, “A grid nesting method for large-eddy simulation of planetary boundary layer flows,” *Boundary-Layer Meteorol.* **80**, 167 (1996).
- ²⁴K. Bech, N. Tillmark, P.H. Alfredsson, and H.I. Andersson, “An investigation of turbulent plane Couette flow at low Reynolds numbers,” *J. Fluid Mech.* **286**, 291 (1995).
- ²⁵J. Komminaho, A. Lundbladh, and A.V. Johansson, “Very large structures in plane turbulent Couette flow,” *J. Fluid Mech.* **320**, 259 (1996).
- ²⁶P. Moin and K. Mahesh, “Direct numerical simulation: A tool in turbulence research,” *Annu. Rev. Fluid Mech.* **30**, 539 (1998).
- ²⁷C.-H. Moeng and P.P. Sullivan, “A comparison of shear and buoyancy driven planetary-boundary-layer flows,” *J. Atmos. Sci.* **51**, 999 (1994).
- ²⁸J.W. Glendening, “Lineal eddy features under strong shear conditions,” *J. Atmos. Sci.* **53**, 3430 (1996).
- ²⁹S. Khanna and J.G. Brasseur, “Three-dimensional buoyancy- and shear-induced local structure of the atmospheric boundary layer,” *J. Atmos. Sci.* **55**, 710 (1998).
- ³⁰J.W. Deardorff, “Numerical investigation of neutral and unstable planetary boundary layers,” *J. Atmos. Sci.* **29**, 91 (1972).
- ³¹J.A. Businger, J.C. Wyngaard, Y. Izumi, and E.F. Bradley, “Flux-profile relationships in the atmospheric surface layer,” *J. Atmos. Sci.* **28**, 181 (1971).
- ³²H. Schlichting, *Boundary-Layer Theory* (McGraw-Hill, New York, 1968) (see discussion on page 268).
- ³³J. Jeong and F. Hussain, “On the identification of a vortex,” *J. Fluid Mech.* **285**, 69 (1995).
- ³⁴D.S. Henn and R.I. Sykes, “Large-eddy simulation of flow over wavy surfaces,” *J. Fluid Mech.* **383**, 75 (1999).
- ³⁵V. De Angelis, P. Lombardi, and S. Banerjee, “Direct numerical simulation of turbulent flow over a wavy wall,” *Phys. Fluids* **9**, 2429 (1997).
- ³⁶A. Smedman, U. Höglström, H. Bergström, A. Rutgersson, K.K. Kahma, and H. Pettersson, “A case study of air-sea interaction during swell conditions,” *J. Geophys. Res.* **104**, 25 833 (1999).
- ³⁷W.J. Plant, “A relationship between wind stress and waveslope,” *J. Geophys. Res.* **87**, 1961 (1982).
- ³⁸P.Y. Li, Ph.D. thesis, York University, 182 pp. (1995).
- ³⁹P.Y. Li, D. Xu, and P.A. Taylor, “Numerical modelling of turbulent airflow over water waves,” *Boundary-Layer Meteorol.* **95**, 397 (2000).
- ⁴⁰C. Mastenbroek, V.K. Makin, M.H. Garat, and J.P. Giovanangeli, “Experimental evidence of the rapid distortion of turbulence in the air flow over water waves,” *J. Fluid Mech.* **318**, 273 (1996).
- ⁴¹G.J. Komen, L. Cavaleri, M. Donelan, K. Hasselmann, S. Hasselmann, and P.A.E.M. Janssen, *Dynamics and Modelling of Ocean Waves* (Cambridge University Press, New York, 1994).
- ⁴²J.F. Meirink and V.K. Makin, “Modeling low-Reynolds-number effects in the turbulent air flow over water waves,” *J. Fluid Mech.* **415**, 155 (2000).

- ⁴³J.A. Harris, S.E. Belcher, and R.L. Street, "Linear dynamics of wind waves in coupled turbulent air-water flow. Part 2. Numerical model," *J. Fluid Mech.* **308**, 219 (1996).
- ⁴⁴J.C. McWilliams, C-H. Moeng, and P.P. Sullivan, "Turbulent fluxes and coherent structures in marine boundary layers: Investigations by large-eddy simulation," in *Air-Sea Exchange: Physics, Chemistry, Dynamics, and Statistics*, edited by G. Geernaert (Kluwer, New York, 1999).
- ⁴⁵C. Johansson, A. Smedman, U. Högstrom, J.G. Brasseur, and S. Khanna, "Critical test of the validity of Monin–Obukhov similarity theory during convective conditions," *J. Atmos. Sci.* **58**, 1549 (2001).